Journal of Power Sources 436 (2019) 226826

Contents lists available at ScienceDirect

Journal of Power Sources

journal homepage: www.elsevier.com/locate/jpowsour

Vertically aligned nanostructured $FeOOH@MnO_2$ core shell electrode with better areal capacitance

Rahul B. Pujari [a], Swati J. Patil [a], Jongsung Park [a], Arunkumar Shanmugasundaram [a], Dong-Weon Lee [a,b,*]

[a] MEMS and Nanotechnology Laboratory, School of Mechanical System Engineering, Chonnam National University, Gwangju, 61186, Republic of Korea
[b] Center for Next-generation Sensor Research and Development, Chonnam National University, Gwangju, 61186, Republic of Korea

HIGHLIGHTS

- 1-D $FeOOH@MnO_2$ core shell nanostructure is prepared by hydrothermal route.
- $FeOOH@MnO_2$ applied for electrochemical charge storage in 0–1 V/AgCl window.
- Electro-active MnO_2 shell supplies electrons and FeOOH nanorods transfer them.
- $FeOOH@MnO_2$ core shell nanostructure shows 0.252 Fcm^{-2} capacitance at 1 $mAcm^{-2}$.
- $FeOOH@MnO_2$//$FeOOH@MnO_2$ SC gives 0.05 $mWhcm^{-2}$ energy and 1.5 $mWcm^{-2}$ power.

GRAPHICAL ABSTRACT

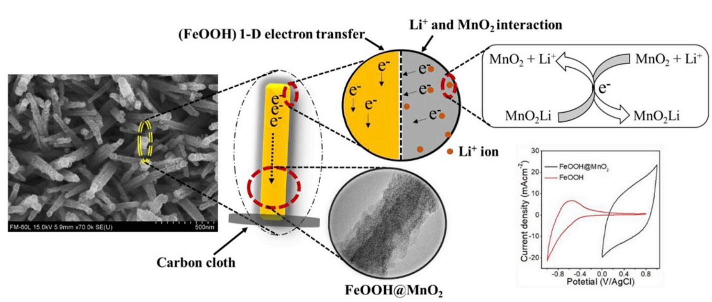

ARTICLE INFO

Keywords:
Areal capacitance
Cyclic voltammetry
Supercapacitor
Energy density
$FeOOH@MnO_2$
Thin film

ABSTRACT

Present work focuses on hydrothermal preparation of $FeOOH@MnO_2$ core shell as a vertically aligned 1-D nanostructure and improvement in electrochemical charge storage by utilizing MnO_2 nanostructure as an active electrode material and vertically aligned FeOOH nanorods for one dimensional electron transfer paths. A $FeOOH@MnO_2$ core shell thin film electrode gives maximum capacitance of 0.252 Fcm^{-2} for the applied current density of 1 $mAcm^{-2}$ and maintains 99.5% capacitance retention for 2000 charge discharge cycles at 5 $mAcm^{-2}$ that attributes to better capacitive charge storage in the material. Assembled solid state symmetric electrochemical capacitor of $FeOOH@MnO_2$ electrode yields maximum of 0.05 $mWhcm^{-2}$ energy density with power delivery of 1.5 $mWcm^{-2}$.

1. Introduction

Supercapacitors or electrochemical capacitors are modern energy storage devices with boosted energy density than dielectric capacitors and higher power density than secondary batteries [1–4]. Pseudocapacitors store higher energy density by the courtesy of higher redox activity metal oxide or conducting polymer electrode materials than electric double layer capacitors (EDLCs), which are formed with electrodes of carbon allotropes such as graphene oxide and carbon nanotubes [5,6]. However, the energy density of pseudocapacitors

* Corresponding author. MEMS and Nanotechnology Laboratory, School of Mechanical System Engineering, Chonnam National University, Gwangju, 61186, Republic of Korea.
E-mail address: mems@jnu.ac.kr (D.-W. Lee).

https://doi.org/10.1016/j.jpowsour.2019.226826
Received 13 March 2019; Received in revised form 24 June 2019; Accepted 27 June 2019
Available online 9 July 2019
0378-7753/

formed with metal oxide electrodes is diminished by small surface area, low electronic conductivity and sluggish electron transfer behaviour [7–11].

Manganese oxide represents most suitable pseudocapacitive material with the low cost of preparation, high theoretical capacitance (1370 F g^{-1}) and wide operating potential window (1.0 V) for MnO_2 polymorph than other metal oxide materials such as NiO (0.5 V) and Co_3O_4 (0.45 V) [12]. However, experimentally achieved capacitances of MnO_2 electrodes are very poor than theoretical value due to the low conductivity of manganese oxide [13–15]. Therefore, different MnO_2 based core shell heterostructures have been fabricated such as $Co_3O_4/SnO_2@MnO_2$ [16], $NiCo_2O_4@MnO_2$ [17], $Co_3O_4@MnO_2$ [18], $ZnO@MnO_2$ [19] and $TiO_2@MnO_2@C$ [20]. In these heterostructures individual constituents help to boost up electrochemical performances of whole core shell electrodes. Recently, $FeOOH@MnO_2$ [21–23] and α-$Fe_2O_3@MnO_x$ [24] core shell nanostructures are extensively studied for improved electrochemical charge storage application. Recent works of core shell $FeOOH@MnO_2$ [22,23] demonstrated either preparation of microstructure material that resulted less active sites available for electrochemical charge storage or preparation of α-$Fe_2O_3@MnO_x$ core shell nanostructure [24] that included low theoretical capacitance MnO_x component in the material. Therefore, $FeOOH@MnO_2$ nanostructure core shell material should be prepared that include more conducting FeOOH core (than Fe_2O_3) and high theoretical capacitance MnO_2 shell material in order to achieve maximum pseudocapacitive charge storage.

This work is focused on direct hydrothermal synthesis of $FeOOH@MnO_2$ 1-D nanostructure core shell material on a carbon cloth substrate for electrochemical charge storage application. For $FeOOH@MnO_2$ core shell nanostructure, individual constituents boost up electrochemical charge storage as; core FeOOH nanorods reduce electron scattering phenomenon and shell MnO_2 nano-layer stores maximum charge storage in the electrode. During electrochemical charge storage in $FeOOH@MnO_2$ electrode, the nanostructured MnO_2 layer serves as an active nano-surface material for electrochemical interactions with lithium (Li^+) ions and the core FeOOH nanorods serve as conductive unidirectional path ways by utilizing low scattering electron transfer phenomenon between MnO_2 and carbon cloth.

2. Experimental work

Analytical reagent iron chloride ($FeCl_3$), sodium sulphate (Na_2SO_4), potassium permanganate ($KMnO_4$), methanol (CH_3OH), hydrochloric acid (HCl) and hydrogen peroxide (H_2O_2) were purchased from Sigma-Aldrich Company. Initially, carbon cloth was activated using 1 M HCl and 30% H_2O_2 advantageous for thin film deposition.

2.1. MnO_2 thin film preparation

MnO_2 thin film was directly prepared on carbon cloth substrate using hydrothermal method. Briefly, diluted solution of methanol was prepared in 30 ml DI water and 0.02 M $KMnO_4$ was added into it under constant magnetic stirring. This final solution was poured in Teflon liner accompanying activated carbon cloth substrate. Then, Teflon liner was sealed in stainless steel autoclave and heated in laboratory oven at 353 K temperature for 1 h. Brown color thin film was formed on carbon cloth substrate after hydrothermal treatment.

2.2. FeOOH thin film preparation

A 0.1 M 15 ml $FeCl_3$ and 0.05 M 15 ml Na_2SO_4 solutions were mixed together, stirred vigorously and transferred to Teflon liner autoclave with activated carbon cloth. Thereafter, sealed autoclave was heated in laboratory oven at 393 K temperature for 6 h and cooled naturally after hydrothermal treatment. Then, yellow color, FeOOH coated carbon cloth substrate was removed from autoclave and washed several times with ethanol to eliminate ionic impurities from the material.

2.3. $FeOOH@MnO_2$ thin film preparation

$FeOOH@MnO_2$ core shell thin film was prepared using second hydrothermal treatment. Initially, a FeOOH coated carbon cloth substrate was kept in diluted methanol solution for 20 min in order to uniform adsorption of methanol solution on FeOOH nanorods. Then, 0.02 M $KMnO_4$ solution was prepared in DI water. Finally, methanol adsorbed FeOOH thin film and $KMnO_4$ solution was transferred to Teflon liner autoclave. Thereafter, sealed autoclave was heated in laboratory oven at 353 K temperature for 1 h. After hydrothermal treatment, brown color $FeOOH@MnO_2$ core shell deposited carbon cloth was removed from autoclave and washed with ethanol repeatedly. Synthesis procedure of $FeOOH@MnO_2$ core shell material on carbon cloth substrate is schematically presented by Fig. S1.

2.4. Characterization of materials

Surface morphology observation and elemental mapping of thin films were carried out using field-emission scanning electron microscopy (FE-SEM) technique with the help of FE-SEM; SU-70, Hitachi High Technologies. Thin films were structurally analysed using X-ray diffractometer (XRD; X'Pert Pro, Malvern Panalytical B.V.) having Cu Kα lines X-ray source and high resolution transmission electron microscopy (HR-TEM; Philips TECNAI F20). Composition and elemental valence states of $FeOOH@MnO_2$ thin film was analysed using X-ray photo emission spectroscopy (XPS) technique with the help of XPS; ESCALab Mark II, VG Scientific Ltd. model. Surface area of $FeOOH@MnO_2$ core shell material was assessed by Brunauer-Emmett-Teller (BET) surface area analysis using a BET, Micromeritics (ASAP2010) model. The electrochemical charge storage analyses of MnO_2 and $FeOOH@MnO_2$ thin film electrodes were carried out using cyclic voltammetry (CV) and galvanostatic charge discharge (GCD) techniques in aqueous 1 M $LiClO_4$ electrolyte. Impedance study of thin film electrodes was performed within frequency range of 0.1–100 kHz at 10 mV ac amplitude.

2.5. Fabrication of symmetric supercapacitor

Symmetric $FeOOH@MnO_2$//$FeOOH@MnO_2$ supercapacitor device was constructed using $FeOOH@MnO_2$ ($1 \times 0.5\ cm^2$) thin film electrode. For solid-state supercapacitor design, PVA-$LiClO_4$ hydrogel was prepared by solution casting method with the composition of 1:1 in 30 ml DI water. As prepared PVA-$LiClO_4$ hydrogel was pasted over two $FeOOH@MnO_2$ electrodes and dried overnight in the ambient conditions. The outer edges of PVA-$LiClO_4$ covered electrodes were sealed by insulating tape for the elimination of direct electrode contact during device fabrication process. Finally, two $FeOOH@MnO_2$ electrodes were formed symmetric $FeOOH@MnO_2$//$FeOOH@MnO_2$ supercapacitor. Similarly, solid state symmetric MnO_2//MnO_2 supercapacitor was also fabricated using two MnO_2 thin film ($1 \times 0.5\ cm^2$) electrodes and PVA-$LiClO_4$ gel electrolyte.

3. Results and discussion

3.1. Physicochemical characterizations of materials

FE-SEM images (Fig. 1 (A and B)) of MnO_2 thin film present nano-sphere like surface morphology on carbon cloth substrate. For FeOOH thin film, FE-SEM images (Fig. 1 (C, D)) show uniform growth of nanorods with average diameter varies from 20 to 100 nm. $FeOOH@MnO_2$ core shell thin film exhibits MnO_2 nano-layer grown on FeOOH nanorods (Fig. 1 (E, F)). Thin nano-coating of MnO_2 material is observed on FeOOH nanorods instead of nano-sphere like surface morphology in case of bare MnO_2 thin film. Thin MnO_2 nano-coating on FeOOH nanorods becomes possible due to long time exposure of FeOOH thin film to methanol solution during experimental design (Fig. S1).

X-ray diffraction study reveals mixed phase (α, γ, β) crystal structure

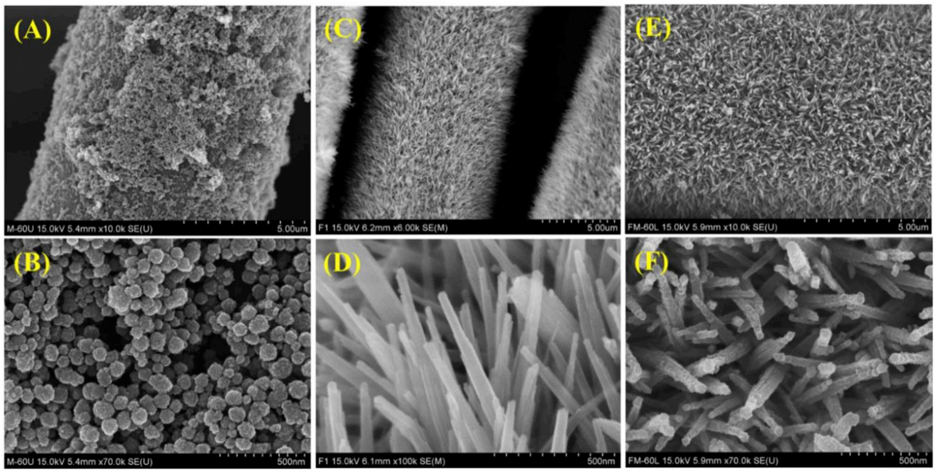

Fig. 1. FE-SEM images of **(A, B)** MnO_2, **(C, D)** FeOOH and **(E, F)** FeOOH@MnO_2 thin films prepared by hydrothermal method.

of manganese oxide (MnO_2) and beta phase of iron oxy-hydroxide (β-FeOOH) presented in Fig. S2 [25–27]. Other two peaks marked as # show presence of γ-FeOOH (JCPDS 01-076-2301) phase, while a single XRD peak dictated by @ with very small intensity correspond to α-Mn_2O_3 (JCPDS, 41–1442) [28,29]. Peaks marked by * correspond to carbon cloth substrate. The XRD peaks for core shell FeOOH@MnO_2 thin film show less intensity than bare MnO_2 thin film. It is due to fine nanosize-coating of MnO_2 material on FeOOH nanorods, as observed in FE-SEM study. Elemental mapping of different elements ((Iron (Fe), manganese (Mn) and oxygen (O 1s)) in FeOOH@MnO_2 sample is presented in Supplementary Fig. S3 in order to test homogeneous distribution of the elements.

Chemical composition and elemental valence states of FeOOH@MnO_2 core shell material is inspected using XPS technique. Survey scan spectrum (Fig. 2 (A)) shows presence of iron, manganese and oxygen elements in the material. Low intensity Fe peaks in the survey scan spectrum attribute to MnO_2 coating on FeOOH nanorods. Additionally, XPS peak observed at 377.6 eV binding energy

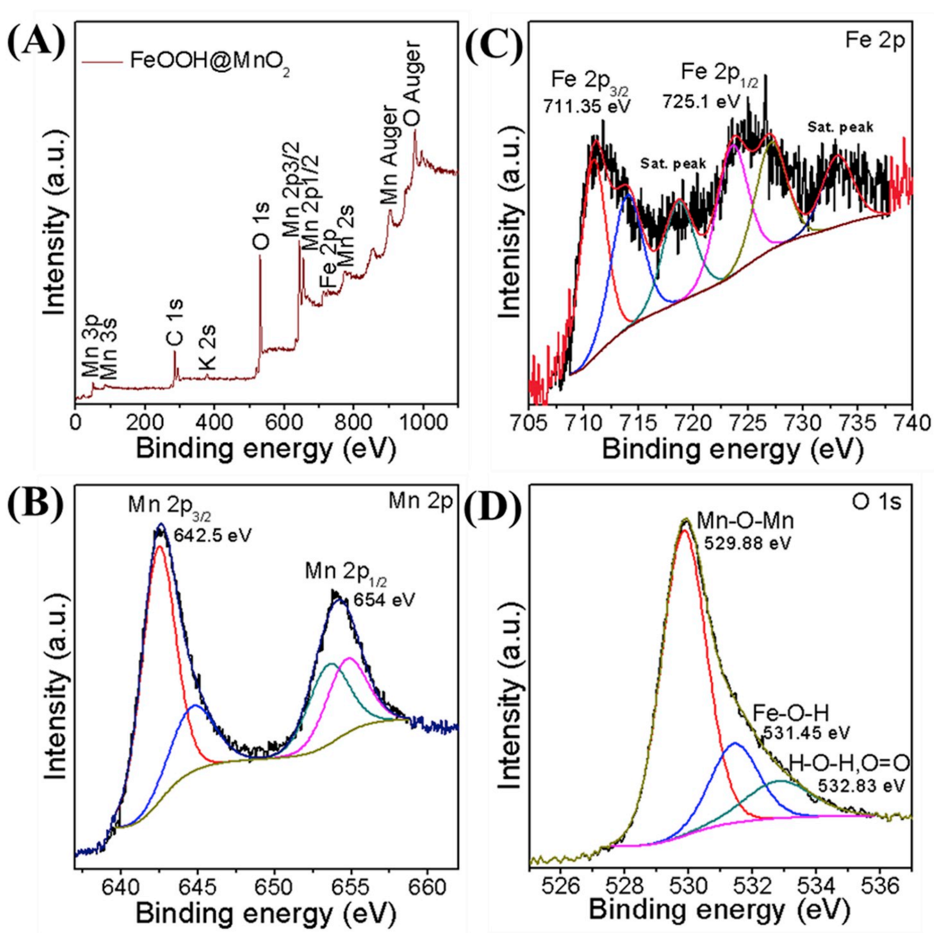

Fig. 2. **(A)** Broad scan survey spectrum of FeOOH@MnO_2 and narrow scan spectra of **(B)** manganese (Mn), **(C)** iron (Fe) and **(D)** oxygen (O) elements.

corresponds to K 2s energy state of ionized potassium [30]. These potassium ions (K^+) from $KMnO_4$ precursor were adsorbed on FeOOH@MnO_2 core shell thin film during MnO_2 growth. $Mn2p_{3/2}$ and $Mn2p_{1/2}$ chemical states of manganese at binding energies of 642.5 and 654 eV dictate MnO_2 phase of manganese oxide Fig. 2 (B) [31]. The XPS peaks at 711.35 and 725.1 eV correspond to energy states of $Fe2p_{3/2}$ and $Fe2p_{1/2}$, respectively with higher energy satellite peaks in Fig. 2 (C) confirms FeOOH phase of material, consistent with the earlier reports [32–34]. A O 1s state of oxygen is de-convoluted into 3 sub-states (Fig. 2 (D)) at the binding energies of 529.88, 531.45 and 532.83 eV that dictate Mn–O–Mn, Fe–O–H and surface adsorbed oxygen (including O_2 and H_2O molecules) bonding, respectively [35,36].

Core shell FeOOH@MnO_2 nanostructure is clearly observed through HR-TEM images (Fig. 3 (A-C)) that show MnO_2 coating on highly crystalline FeOOH nanorods consistent with FE-SEM results. Fig. 3 (D and E) show fast fourier transform (FFT) patterns obtained from HR-TEM images of MnO_2 and FeOOH@MnO_2, respectively. Selected area electron diffraction (SAED) patterns dictate crystal orientations of bare MnO_2 and FeOOH@MnO_2. Ring pattern of MnO_2 material (Fig. 3 (F)) shows presence of (101), (200) and (211) planes. For FeOOH@MnO_2 core shell nanostructure (Fig. 3 (G)), dot pattern co-existes with ring pattern, which is evidence of core shell FeOOH@MnO_2 nanostructure. In Fig. 3 (G), two adjacent dots dictate (120) and (251) planes of crystalline FeOOH nanorods, consistent with the XRD results.

Surface area of FeOOH@MnO_2 material is obtained by Brunaeur-Emmett-Teller (BET) surface area method using N_2 adsorption-desorption isotherm (Fig. S4 (A)). FeOOH@MnO_2 exhibited Brunauer-Deming-Deming-Teller (BDDT) data with the characteristic feature of type IV isotherm and H3-type hysteresis loop that suggests presence of mesopores in the material.

The pore size distribution in FeOOH@MnO_2 material is evaluated via Barrett-Joyner-Halenda (BJH) model (Fig. S4 (B)) that shows occupancy of meso-pores in the range of 2.44–50 nm and BET specific surface area of FeOOH@MnO_2 is calculated to be 300 $m^2\,g^{-1}$. Such a high surface area FeOOH@MnO_2 material with meso-porous structure can be fully utilized for electrochemical aqueous supercapacitor application, as mesopores are easily accessible for solvated lithium ions. However, material with micro (pore size < 2 nm) and/or macro pore structure (pore size > 50 nm) hinders electrochemical performance due to inaccessible pores and/or low specific surface area of material, respectively.

3.2. Electrochemical charge storage analyses

Fig. 4 (A, B) present CV curves at 5 to 100 mVs^{-1} scan rates of MnO_2 and FeOOH@MnO_2 electrodes, respectively that show better rectangular nature of CV curves for FeOOH@MnO_2 electrode. Moreover, FeOOH@MnO_2 electrode shows higher integrated area of CV loops suitable for higher charge storage than bare MnO_2 electrode. All CV curves show nearly rectangular shapes without obvious redox peaks indicative of surface pseudocapacitive charge storage of both the electrodes in $LiClO_4$ electrolyte. The symmetrical charging and discharging of CV curves of both electrodes suggest higher columbic efficiency of material [37]. Following reversible reaction is responsible for charge storage at the surface of MnO_2 nanoparticles due to Mn (IV) and Mn (III) redox transitions [38,39],

$$MnO_2 + Li^+ + e^- \leftrightarrow MnO_2Li \quad (1)$$

Comparative CV curves of FeOOH and FeOOH@MnO_2 electrodes are recorded (Fig. S5) in positive potential window (0 to + 1.0 V/AgCl) in order to demonstrate charge storage of both the electrodes. It demonstrates that for FeOOH@MnO_2 core shell electrode, mainly MnO_2 nanoparticles take part in redox activity by utilizing reversible reactions shown in equation (1) and FeOOH nanorods mainly serve for instantaneous transfer of electrons between MnO_2 nanoparticles and current collector (carbon cloth), which helps to reduce electron scattering phenomenon in the electrode (Fig. 5). More insights on charge storage mechanism of both FeOOH@MnO_2 and MnO_2 electrodes in $LiClO_4$ electrolyte are provided in Fig. S6. The generalised equation between current responses versus scan rates of CV curve for infinitesimal diffusion process is given by following equation,

$$I = av^b \quad (2)$$

where, a, b are adjusting parameters; I and v are current response at 0.6 V/AgCl potential and scan rate for a CV curve, respectively. For $b = 1.0$ value, surface capacitive charge storage is expected for the electrode, corresponding to double layer electrostatic and/or surface pseudocapacitive reversible reactions, while $b = 0.5$ predicts charge storage is influenced by diffusion mechanism of electrolyte ions through electrode matrix. Both MnO_2 and FeOOH@MnO_2 electrodes exhibit surface pseudocapacitive type charge storage indicated by 0.93 and 0.89 slope (b) values, respectively obtained for log (i) versus log (v) plots of both electrodes (Fig. S6).

The recorded GCD curves of both MnO_2 and FeOOH@MnO_2 electrodes (Fig. 4 (C, D)), respectively show symmetrical shape for charging and discharging that suggests better columbic efficiency of the electrodes. Areal capacitances of MnO_2 and FeOOH@MnO_2 electrodes are calculated using following equation,

$$\text{Areal capacitance} = \frac{I_d \times t_d}{V \times A} \quad (3)$$

where, I_d, t_d, V and A are designated as magnitude of applied current density, discharging time, applied potential window and 1 cm^2 area of electrode, respectively. The highest 0.252 Fcm^{-2} areal capacitance is obtained for FeOOH@MnO_2 core shell electrode in comparison with

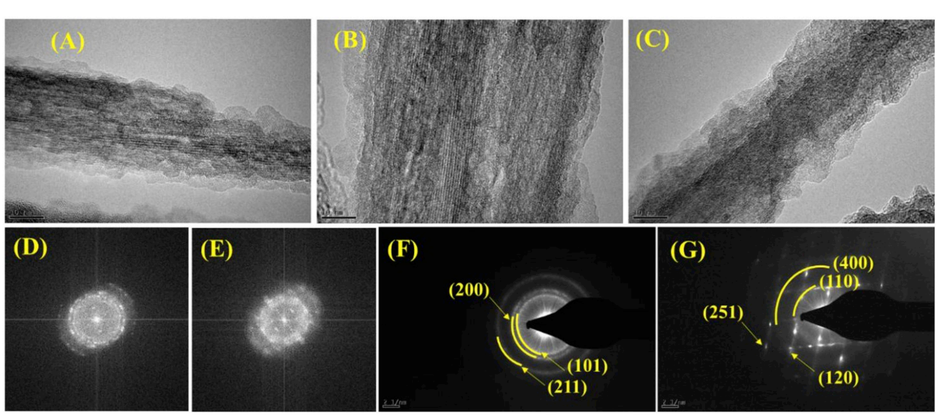

Fig 3. **(A–C)** HR-TEM images of FeOOH@MnO_2 nanorods, FFT patterns of **(D)** MnO_2 and **(E)** FeOOH@MnO_2 core shell and selected area diffraction patterns of **(F)** MnO_2 and **(G)** FeOOH@MnO_2.

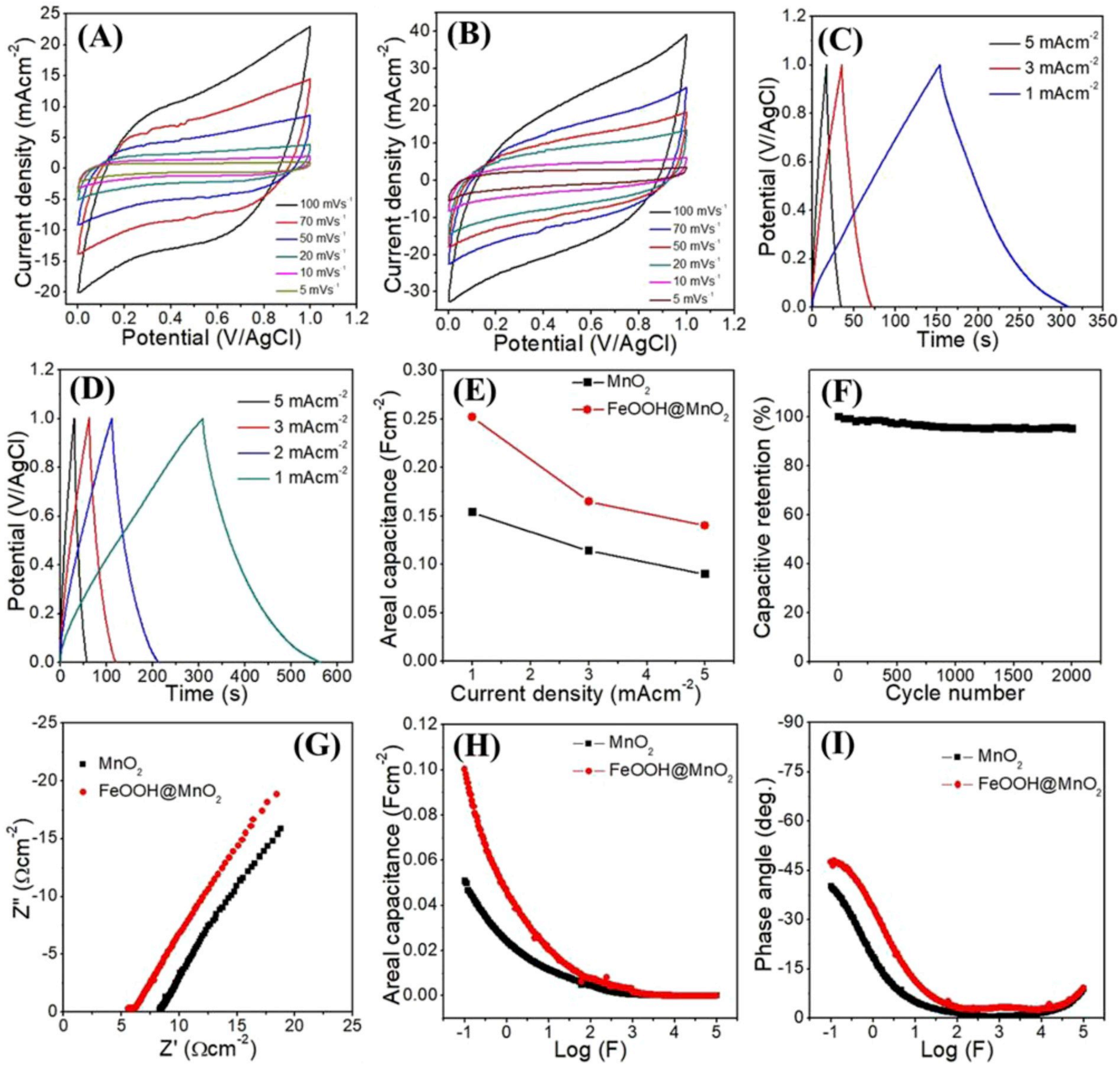

Fig. 4. CV curves of **(A)** MnO_2 and **(B)** FeOOH@MnO_2 electrodes recorded at different scan rates. **(C)** and **(D)** are GCD curves of MnO_2 and FeOOH@MnO_2, respectively. **(E)** Comparative plots of areal capacitances of MnO_2 and FeOOH@MnO_2 electrodes versus different current densities, **(F)** capacitive retention of FeOOH@MnO_2 electrode over 2000 charge discharge cycles scanned at 5 $mAcm^{-2}$ current density, **(G)** impedance spectra of electrodes within 0.1–100 kHz frequency range, **(H)** comparative areal capacitances and **(I)** phase angle relation with applied frequency range of 0.1–100 kHz.

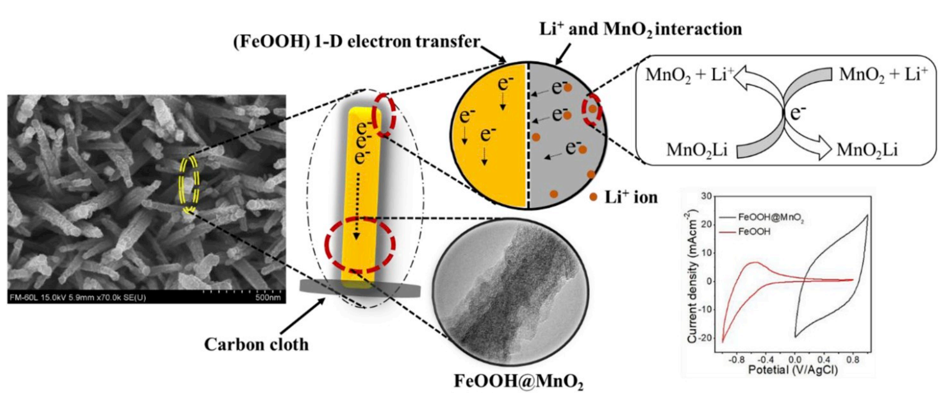

Fig. 5. Schematic representation for electrochemical charge storage and electron transfer phenomenon of FeOOH@MnO_2 core shell electrode in aqueous 1 M $LiClO_4$ electrolyte.

0.153 Fcm^{-2} for bare MnO_2 at the applied current density of 1 $mAcm^{-2}$ seen in Fig. 4 (E). FeOOH@MnO_2 electrode still retains 0.140 Fcm^{-2} capacitance at high current density of 5 $mAcm^{-2}$. In order to examine, whether carbon cloth substrate contributes for any capacitance, CV and GCD curves are recorded at 100 mVs^{-1} scan rate and 1 $mAcm^{-2}$ current density, respectively (Fig. S7). For carbon cloth, integrated area of closed CV loop and discharging time in GCD curve are negligible quantities (less than 1%) compared with FeOOH@MnO_2 core shell electrode. It indicates negligible capacitance contribution of carbon cloth substrate in the performance of FeOOH@MnO_2 thin film electrode.

The improvement in capacitance of core shell electrode is achieved by utilizing high surface area (300 $m^2 g^{-1}$) of electrode and fast instantaneous electron transfer phenomenon via vertically grown FeOOH nanorods. The achieved capacitance in present work for FeOOH@MnO_2 core shell electrode is higher than 0.227 Fcm^{-2} obtained by Sarkar et al. [24] for α-Fe_2O_3@MnO_x electrode at 0.5 $mAcm^{-2}$ current density.

Cyclic lifetime of FeOOH@MnO_2 electrode is performed for continuous 2000 C V cycles that exhibits excellent 99.5% (Fig. 4 (F)) capacitive retention, which is indicative of good reversibility of active electrode material. The comparative impedance spectra (Fig. 4 (G)) of MnO_2 and FeOOH@MnO_2 electrodes present lowered equivalent series resistance (ESR) (5.5 Ωcm^{-2}) for FeOOH@MnO_2 electrode than MnO_2 (8.2 Ωcm^{-2}). It signifies to unidirectional transfer of electrons via FeOOH nanorods towards current collector resulting less electron scattering phenomenon in FeOOH@MnO_2 electrode. Areal capacitance response in Fig. 4 (H) of FeOOH@MnO_2 core shell electrode exhibits higher capacitance (0.105 Fcm^{-2}) at 0.1 Hz frequency of ac signal compared to 0.051 Fcm^{-2} for MnO_2 electrode. Similarly, phase angle response (Fig. 4 (I)) shows better supercapacitive behaviour for core shell FeOOH@MnO_2 electrode, while for MnO_2 case it becomes more resistive in lower frequency region.

The constructed solid state symmetric FeOOH@MnO_2// FeOOH@MnO_2 supercapacitor is evaluated for electrochemical charge storage within operating potential window of 0 to +1.0 V. Symmetrical CV (Fig. 6 (A)) and GCD (Fig. 6 (B)) curves of FeOOH@MnO_2// FeOOH@MnO_2 supercapacitor at different scan rates and currents, respectively exhibit better coulombic efficiency of the device. Highest areal capacitance of 0.135 F is obtained for the device at 0.5 mA current seen in Fig. 6 (C). Ragone plot of FeOOH@MnO_2//FeOOH@MnO_2 supercapacitor (Fig. 6 (D)) shows highest energy density of 0.05 $mWhcm^{-2}$ for corresponding power density of 1.5 $mWcm^{-2}$. Cyclic lifetime of supercapacitor is tested for 2000 GCD cycles at 2 $mAcm^{-2}$ current that shows 94.5% capacitive retention in the device seen in Fig. 6 (E). Impedance spectrum (Fig. 6 (F)) exhibits better supercapacitive feature of the device, as Nyquist plot have low impedance values along the diagonal of plot in low frequency region. Areal capacitance and phase angle responses (Fig. S8) of FeOOH@MnO_2// FeOOH@MnO_2 supercapacitor dictate better rate capability and supercapacitive nature with varied high to low frequency range of ac signal.

Similarly, symmetric MnO_2//MnO_2 supercapacitor is also studied for charge storage evaluation (Fig. S9) using CV and GCD techniques within operating potential window of 0 to +1.0 V. Rectangular CV curves without obvious redox peaks at each scan rates show pseudocapacitive charge storage in the device. The highest 0.102 F areal capacitance of MnO_2//MnO_2 supercapacitor is obtained at 0.5 mA current, which is higher than 0.047 Fcm^{-2} reported for typical MnO_2//MnO_2 supercapacitor by Wang et al. [40]. The highest 0.035 $mWhcm^{-2}$ energy density and 1.25 $mWcm^{-2}$ power density are obtained for MnO_2//MnO_2 supercapacitor. Cyclic lifetime of device is tested for 2000 GCD cycles at 2 $mAcm^{-2}$ current that shows 90% capacitive retention of device after cycling process.

4. Conclusions

Core shell 1-dimensional FeOOH@MnO_2 nanostructure thin film electrode have been successfully deposited on carbon cloth substrate by hydrothermal method. Maximum electrochemical charge storage of FeOOH@MnO_2 electrode is achieved by MnO_2 nano-layer coating on vertically grown FeOOH nanorods. MnO_2 nano-layer is used as an electro-active electrode, while FeOOH nanorods served for low electron

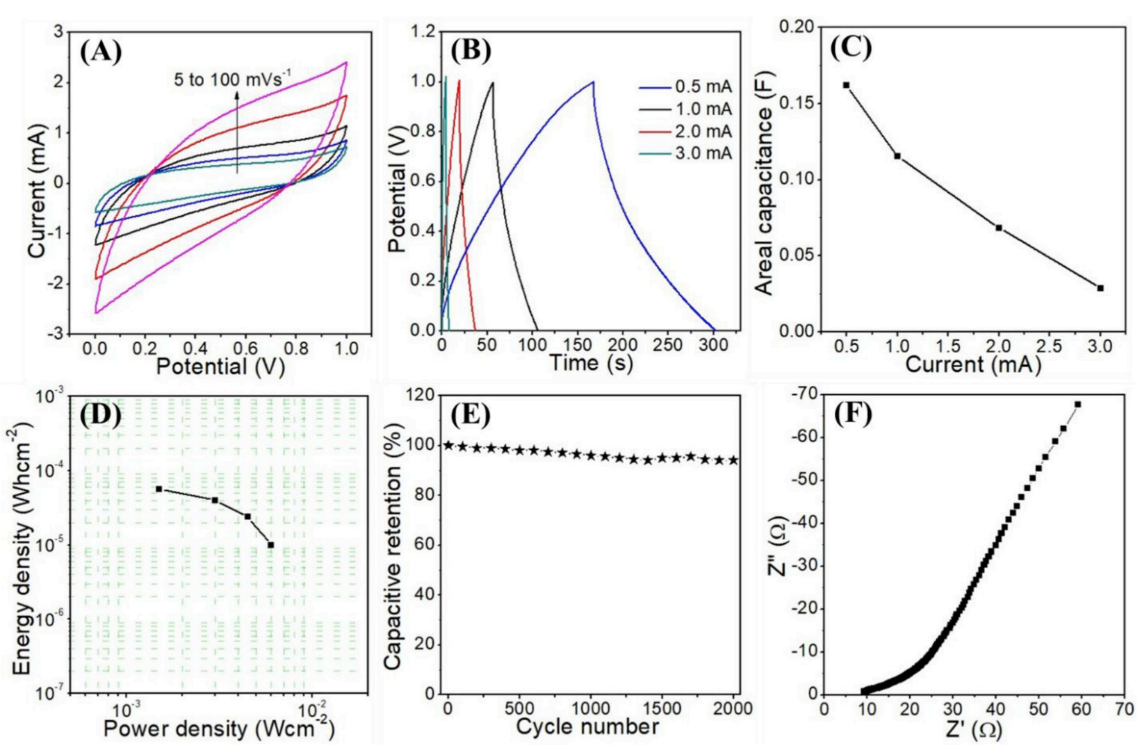

Fig. 6. **(A)** CV curves, **(B)** GCD curves, **(C)** areal capacitances, **(D)** Ragone plot, **(E)** capacitive retention for 2000 GCD cycles and **(F)** impedance spectrum of symmetric FeOOH@MnO_2//FeOOH@MnO_2 supercapacitor.

scattering phenomenon useful for charge conduction. Thus, present synthesis strategy synergistically improved areal capacitance of $FeOOH@MnO_2$ core shell electrode. Therefore, assembled core shell electrode based symmetric $FeOOH@MnO_2//FeOOH@MnO_2$ supercapacitor exhibited better 0.05 $mWhcm^{-2}$ energy density and 1.5 $mWcm^{-2}$ power density and demonstrated $FeOOH@MnO_2$ nanostructure core shell electrode suitable for supercapacitor application. Similar synthesis strategy can be applied for other metal oxides such as cobalt oxide and nickel oxide for enhancement in their areal capacitances.

Acknowledgement

This study was supported by the National Research Foundation of Korea grant funded by the Korea government (MSIP) (No.2015R1A4A1041746).

Appendix A. Supplementary data

Supplementary data to this article can be found online at https://doi.org/10.1016/j.jpowsour.2019.226826.

References

[1] X. Lu, Y. Zeng, M. Yu, T. Zhai, C. Liang, S. Xie, M.S. Balogun, Y. Tong, Oxygen-deficient hematite nanorods as high-performance and novel negative electrodes for flexible asymmetric supercapacitors, Adv. Mater. 26 (2014) 3148–3155.
[2] P. Ge, S. Li, H. Shuai, W. Xu, Y. Tian, L. Yang, G. Zou, H. Hou, X. Ji, Engineering 1D chain-like architecture with conducting polymer towards ultra-fast and high-capacity energy storage by reinforced pseudocapacitance, Nano Energy 54 (2018) 26–38.
[3] H. Liang, C. Xia, A.H. Emwas, D.H. Anjum, X. Miao, H.N. Alshareef, Phosphine plasma activation of α-Fe_2O_3 for high energy asymmetric supercapacitors, Nano Energy 49 (2018) 155–162.
[4] Z. Ma, G. Shao, Y. Fan, G. Wang, J. Song, D. Shen, Construction of hierarchical α-MnO_2 nanowires@ultrathin δ-MnO_2 nanosheets core-shell nanostructure with excellent cycling stability for high-power asymmetric supercapacitor electrodes, ACS Appl. Mater. Interfaces 8 (2016) 9050–9058.
[5] W. Gong, B. Fugetsu, Z. Wang, I. Sakata, L. Su, X. Zhang, H. Ogata, M. Li, C. Wang, J. Li, J.O. Medina, M. Terrones, M. Endo, Carbon nanotubes and manganese oxide hybrid nanostructures as high performance fiber Supercapacitors, Commun. Chem. 1 (2018) 16.
[6] B. Xie, M. Yu, L. Lu, H. Feng, Y. Yang, Y. Chen, H. Cui, R. Xiao, J. Liu, Pseudocapacitive Co_9S_8/graphene electrode for high-rate hybrid supercapacitors, Carbon 141 (2019) 134–142.
[7] H.S. Kim, J.B. Cook, H. Lin, J.S. Ko, S.H. Tolbert, V. Ozolins, B. Dunn, Oxygen vacancies enhance pseudocapacitive charge storage properties of MoO_{3-x}, Nat. Mater. 16 (2017) 454–460.
[8] G. Nie, X. Lu, M. Chi, Y. Zhu, Z. Yang, N. Song, C. Wang, Hierarchical α-Fe_2O_3@MnO_2 core-shell nanotubes as electrode materials for high-performance supercapacitors, Electrochim. Acta 231 (2017) 36–43.
[9] X.F. Lu, X.Y. Chen, W. Zhou, Y.X. Tong, G.R. Li, α-Fe_2O_3@PANI core-shell nanowire arrays as negative electrodes for asymmetric supercapacitors, ACS Appl. Mater. Interfaces 7 (2015) 14843–14850.
[10] L. Wang, H. Yang, X. Liu, R. Zeng, M. Li, Y. Huang, X. Hu, Constructing hierarchical tectorum-like α-Fe_2O_3/Ppy nanoarrays on carbon cloth for solid-state asymmetric supercapacitors, Angew. Chem. Int. Ed. 56 (2017) 1105–1110.
[11] S. Sun, T. Zhai, C. Liang, S.V. Savilov, H. Xi, Boosted crystalline/amorphous $Fe_2O_{3-\delta}$ core/shell heterostructure for flexible solid-state pseudocapacitors in large scale, Nano Energy 45 (2018) 390–397.
[12] Y. Hu, Y. Wu, J. Wang, Manganese-oxide-based electrode materials for energy storage applications: how close are we to the theoretical capacitance? Adv. Mater. 30 (2018) 1802569.
[13] S. Zhu, L. Li, J. Liu, H. Wang, T. Wang, Y. Zhang, L. Zhang, R.S. Ruoff, F. Dong, Structural directed growth of ultrathin parallel birnessite on β-MnO_2 for high-performance asymmetric supercapacitors, ACS Nano 12 (2018) 1033–1042.
[14] E. Umeshbabu, P. Justin, G.R. Rao, Tuning the surface morphology and pseudocapacitance of MnO_2 by a facile green method employing organic reducing sugars, ACS Appl. Energy Mater. 1 (2018) 3654–3664.
[15] R. Rajagopal, K.S. Ryu, Influence of rare earth elements on porosity controlled synthesis of MnO_2 nanostructures for supercapacitor applications, Electrochim. Acta 265 (2018) 532–546.
[16] M. Huang, X.L. Zhao, F. Li, W. Li, B. Zhang, Y.X. Zhang, Synthesis of Co_3O_4/SnO_2@MnO_2 core-shell nanostructures for high-performance supercapacitors, J. Mater. Chem. 3 (2015) 12852–12857.
[17] Y. Zhang, B. Wang, F. Liu, J. Cheng, X.W. Zhang, L. Zhang, Full synergistic contribution of electrodeposited three-dimensional $NiCo_2O_4$@MnO_2 nanosheet networks electrode for asymmetric supercapacitors, Nano Energy 27 (2016) 627–637.
[18] D. Kong, J. Luo, Y. Wang, W. Ren, T. Yu, Y. Luo, Y. Yang, C. Cheng, Three-dimensional Co_3O_4@MnO_2 hierarchical nanoneedle arrays: morphology control and electrochemical energy storage, Adv. Funct. Mater. 24 (2014) 3815–3826.
[19] A.V. Radhamani, K.M. Shareef, M.S.R. Rao, ZnO@MnO_2 core-shell nanofiber cathodes for high performance asymmetric supercapacitors, ACS Appl. Mater. Interfaces 844 (2016) 30531–30542.
[20] D. Shin, J. Shin, T. Yeo, H. Hwang, S. Park, W. Choi, Scalable synthesis of triple-core shell nanostructures of TiO_2@MnO_2@C for high performance supercapacitors using structure-guided combustion waves, Small 14 (2018) 1703755.
[21] J. Yang, H. Wang, R. Wang, Facile synthesis of core-shell FeOOH@MnO_2 nanomaterials with excellent cycling stability for supercapacitor electrodes, J. Mater. Sci. Mater. Electron. 28 (2017) 6481–6487.
[22] K. Du, G. Wei, F. Zhao, C. An, H. Wang, J. Li, C. An, Urchin-like FeOOH hollow microspheres decorated with MnO_2 for enhanced supercapacitor performance, Sci. Chin. Mater. 16 (2018) 48–56.
[23] Y. Lv, H. Che, A. Liu, J. Mu, C. Dai, X. Zhang, Y. Bai, G. Wang, Z. Zhang, Urchin-like α-FeOOH@MnO_2 core-shell hollow microspheres for high-performance supercapacitor electrode, J. Appl. Electrochem. 47 (2017) 433–444.
[24] D. Sarkar, S. Pal, S. Mandal, A. Shukla, D.D. Sarma, α-Fe_2O_3-based core-shell-nanorod-structured positive and negative electrodes for a high-performance α-Fe_2O_3/c//α-Fe_2O_3/MnOx asymmetric supercapacitor, J. Electrochem. Soc. 164 (2017) A2707–A2715.
[25] L.F. Chen, Z.Y. Yu, J.J. Wang, Q.X. Li, Z.Q. Tan, Y.W. Zhu, S.H. Yun, Metal-like fluorine-doped β-FeOOH nanorods grown on carbon cloth for scalable high-performance supercapacitors, Nano Energy 11 (2015) 119–128.
[26] Y.X. Zhang, Y. Ji, A facile solution approach for the synthesis of akaganeite (β-FeOOH) nanorods and their ion-exchange mechanism toward as (V) ions, Appl. Surf. Sci. 290 (2014) 102–106.
[27] T. Zhu, W.L. Ong, L. Zhu, G.W. Ho, TiO_2 fibers supported β-FeOOH nanostructures as an efficient visible light photocatalyst and room temperature sensor, Sci. Rep. 5 (2015) 1–15.
[28] Y.C. Chen, Y.G. Lin, Y.K. Hsu, S.C. Yen, K.H. Chen, L.C. Chen, Novel iron oxyhydroxide lepidocrocite nanosheet as ultrahigh power density anode material for asymmetric supercapacitors, Small 10 (2014) 3803–3810.
[29] J. Wang, G. Zhu, L. Deng, L. Kang, Z. Hao, Z. Liu, Novel synthesis and formation process of uniform Mn_2O_3 cubes, CrystEngComm 14 (2012) 8253–8260.
[30] F. Qian, X. Li, L. Tang, S.K. Lai, C. Lu, S.P. Lau, Potassium doping : tuning the optical properties of graphene quantum dots, AIP Adv. 6 (2016) 75116.
[31] Y. Wang, Y.Z. Zhang, D. Dubbink, J.E. Elshof, Inkjet printing of δ-MnO_2 nanosheets for flexible solid-state microsupercapacitor, Nano Energy 49 (2018) 481–488.
[32] Q. Lu, L. Liu, S. Yang, J. Liu, Q. Tian, W. Yao, Q. Xue, M. Li, W. Wu, Facile synthesis of amorphous FeOOH/MnO_2 composites as screen printed electrode materials for all-printed solid-state flexible supercapacitors, J. Power Sources 361 (2017) 31–38.
[33] X. Gong, S. Li, P.S. Lee, A fiber asymmetric supercapacitor based on FeOOH/Ppy on carbon fibers as an anode electrode with high volumetric energy density for wearable applications, Nanoscale 9 (2017) 10794–10801.
[34] J. Chen, J. Xu, S. Zhou, N. Zhao, C.P. Wong, Amorphous nanostructured FeOOH and Co-Ni double hydroxides for high-performance aqueous asymmetric supercapacitors, Nano Energy 21 (2016) 145–153.
[35] J. Ma, Q. Zhao, D. Wei, H. Liu, X. Wang, Z. Chen, J. Wang, Simple construction of core-shell MnO_2@TiO_2 with highly enhanced U(VI) adsorption performance and evaluated adsorption mechanism, Inorg. Chem. Front. 6 (2019) 1011–1021.
[36] T. Yang, L. Meng, S. Han, J. Hou, S. Wang, X. Wang, Simultaneous reductive and sorptive removal of Cr(VI) by activated carbon supported β-FeOOH, RSC Adv. 7 (2017) 34687–34693.
[37] V. Augustyn, P. Simon, B. Dunn, Pseudocapacitive oxide materials for high-rate electrochemical energy storage, Energy Environ. Sci. 7 (2014) 1597–1614.
[38] Y. Song, T. Liu, M. Li, B. Yao, T. Kou, D. Feng, F. Wang, Y. Tong, X.X. Liu, Y. Li, Engineering of mesoscale pores in balancing mass loading and rate capability of hematite films for electrochemical capacitors, Adv. Energy Mater. 8 (2018) 1801784.
[39] X. Liang, K. Chen, D. Xue, A flexible and ultrahigh energy density capacitor via enhancing surface/interface of carbon cloth supported colloids, Adv. Energy Mater. 8 (2018) 1703329.
[40] Y. Wang, W. Zhou, Q. Kang, J. Chen, Y. Li, X. Feng, D. Wang, Y. Ma, W. Huang, Patterning island-like MnO_2 arrays by breath figure templates for flexible transparent supercapacitors, ACS Appl. Mater. Interfaces 10 (2018) 27001–27008.